Imaging Glaucomatous Damage Across the Temporal Raphe

Gang Huang, Ting Luo, Thomas J. Gast, Stephen A. Burns, Victor E. Malinovsky, and William H. Swanson

School of Optometry, Indiana University, Bloomington, Indiana, United States

Correspondence: Stephen A. Burns, School of Optometry, Indiana University Bloomington, 800 East Atwater Avenue, Bloomington, IN 47405-3635, USA; staburns@indiana.edu.

Submitted: February 22, 2015
Accepted: April 7, 2015

Citation: Huang G, Luo T, Gast TJ, Burns SA, Malinovsky VE, Swanson WH. Imaging glaucomatous damage across the temporal raphe. *Invest Ophthalmol Vis Sci*. 2015;56:3496–3504. DOI:10.1167/iovs.15-16730

Purpose. To image and analyze anatomical differences at the temporal raphe between normal and glaucomatous eyes using adaptive optics scanning laser ophthalmoscopy (AOSLO) and optical coherence tomography (OCT), and to relate these differences to visual field measurements.

Methods. Nine glaucomatous eyes of 9 patients (age 54–78 years, mean deviation of visual field [MD] −5.03 to −0.20 dB) and 10 normal eyes of 10 controls (age 54–81, MD −1.13 to +1.39 dB) were enrolled. All the participants were imaged in a region that was centered approximately 9° temporal to the fovea. The size of imaging region was at least 10° vertically by 4° horizontally. The raphe gap, defined as the distance between the superior and inferior retinal nerve fiber layer (RNFL) bundles, was measured. A bundle index was computed to quantify the relative reflectivity and density of the nerve fiber bundles. We also measured thickness of the ganglion cell complex (GCC) and RNFL.

Results. The raphe gap was larger in glaucomatous eyes than control eyes. Specifically, eight glaucomatous eyes with local averaged field loss no worse than −3.5 dB had larger raphe gaps than all control eyes. The bundle index, GCC thickness, and RNFL thickness were on average reduced in glaucomatous eyes, with the first two showing statistically significant differences between the two groups.

Conclusions. Structural changes in the temporal raphe were observed and quantified even when local functional loss was mild. These techniques open the possibility of using the raphe as a site for glaucoma research and clinical assessment.

Keywords: raphe, glaucoma, adaptive optics, visual field, OCT

Glaucoma is a group of blinding optic neuropathies that represent a major irreversible cause of vision loss in the elderly. The disease is characterized by damage to the ganglion cells and their axons and a resulting thinning of the retinal nerve fiber layer (RNFL) and cupping of the optic disc. The damage leads to a related loss in visual function.

Because the vision loss resulting from glaucoma is irreversible, it is important to detect glaucoma in its early stages and to carefully monitor status as the disease progresses. In practice, this requires both functional and structural measurements. The current "gold" standard for testing visual function is visual field testing performed using static automated perimetry (SAP). For a given eye, visual sensitivity is measured at discrete retinal locations, and compared with normative values. As glaucoma progresses, the visual defects often appear in certain distinct locations; for instance, arcuate defects, paracentral scotomas, and nasal steps. A major disadvantage of visual field testing is that there is large individual variability,[1–3] and this variability, because it lowers the sensitivity for detecting glaucoma, has led to an increased emphasis on measurements of changes to retinal structure as a complement to visual field testing.

Traditionally, structural measures of glaucomatous damage relied on fundus cameras and confocal scanning laser ophthalmoscopy (SLO) for evaluating the optic disc and imaging RNFL defects,[4–10] and scanning laser polarimetry for evaluation of the peripapillary RNFL.[11] Recently, optical coherence tomography (OCT) has been increasingly used to detect and monitor glaucomatous damage to the RNFL,[12] because of its high axial resolution and ability to quantify changes in the thickness of individual retinal layers. Another technique that was brought to the retinal imaging field is adaptive optics (AO) imaging, which allows for high-resolution retinal imaging without degradation by ocular aberrations.[13] Adaptive optics retinal imaging has been used for investigation of glaucomatous damage of nerve fiber bundles in human eyes.[14,15] However, most of current imaging-based measures were applied near the optic disc, where the RNFL is the thickest. Imaging at this location has the advantage that all ganglion cell axons must exit the eye at the optic disc, so the analysis can concentrate on this area and provide a summed measure of the axons. However, it also has the disadvantage that although there are general spatial relations between locations in the visual field and the thickness of the RNFL at particular portions of the optic disc and peripapillary region, there is large individual variability in this relation and so relating a particular structural measurement to a particular region of the visual field can be challenging.[16–23]

An apparent solution is to look at structural changes to the RNFL closer to the locations of the measured visual field defects. One portion of the retina where this becomes possible is near the temporal raphe in the temporal retina. In this region, the ganglion cell axons are first incorporated into axon bundles, and then course across the retina toward the optic disc. For eccentricities approximately 9° temporal to the fovea,

the ganglion cells have relatively small displacement from the position of their cone inner segments, and thus there is a close spatial relation between the local sensitivity and the local RNFL.[24,25] This region also has an advantage for studying the relation of early structural and functional loss because the raphe region is believed to be one of the major sites where early visual function abnormalities appear.[26–29]

Unfortunately most clinical techniques cannot measure the RNFL reliably near the raphe because the RNFL is relatively thin and has low contrast. In the past few years, efforts have been made to image and measure the RNFL in this region using high-resolution imaging techniques. In particular, the AO scanning laser ophthalmoscope (AOSLO) has demonstrated the ability to image the temporal raphe in healthy young subjects.[30,31] Similarly, the latest OCT techniques have been demonstrated to image the temporal raphe.[32]

The current study used an AOSLO to measure en face structure of the RNFL near the raphe and a commercial OCT to measure the thickness of the RNFL and ganglion cell complex (GCC) in the same region, and related these measurements to visual sensitivity as measured using SAP in patients with glaucoma and healthy control subjects.

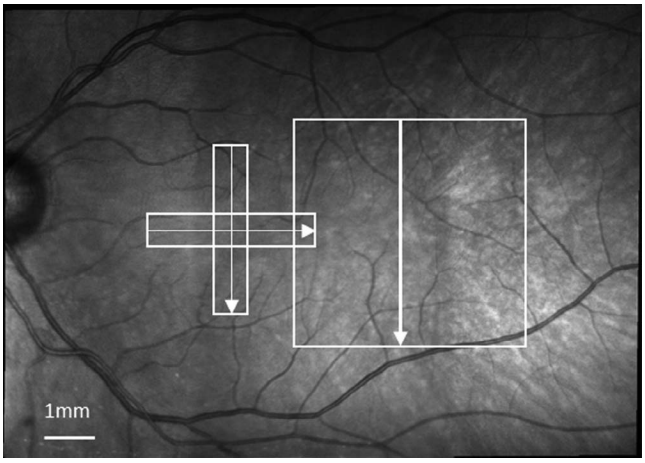

Figure 1. A fundus mosaic constructed from two 30° × 30° wide-field SLO images, using the Heidelberg built-in software. The *white boxes* in the mosaic indicate the regions and directions (*arrows*) of OCT scans. The two orthogonal OCT volume scans were centered on the fovea. The third volume scan was centered at approximately 12° temporal to the fovea.

Methods

Subjects

For the current study, we selected 9 glaucomatous eyes of 9 patients (54–78 years old, mean 65.6 years, SD 6.7; four men and five women) and 10 control eyes of 10 age-similar subjects (54–81 years, mean 66.3 years old, SD 6.8; five men and five women). All these subjects were drawn from the subject pool of a recently completed multicenter glaucoma longitudinal study,[33] which adhered to the tenets of the Declaration of Helsinki and was approved by the institutional review boards at SUNY College of Optometry and at Indiana University. Common inclusion criteria for both groups were the following: best corrected visual acuity of 20/20 or better (20/25 for subjects older than 70), spherical equivalent within −6 diopters (D) to +2 D, cylinder correction less than 3 D, absence of known ocular or systemic disease known to affect the visual field (except for glaucoma in the patient group), and history of reliable visual fields. Common exclusion criteria for both groups were failure of pupil dilation, significant cataract, or inability to stably fixate for OCT or AOSLO imaging.

All patients had abnormal-appearing discs consistent with glaucoma, both on clinical examinations and OCT images. Among these nine glaucomatous eyes, seven eyes had asymmetric visual field sensitivity loss across the horizontal midline in the nasal field and two eyes had no visual field loss in the nasal field. The mean deviation of visual field (MD) ranged from −5.03 dB to −0.20 dB (mean −1.88 ± 1.64 dB) in the glaucoma group, and ranged from −1.13 dB to +1.39 dB (mean 0.03 ± 0.64 dB) in the control group (see Supplementary Appendix). The vertical cup/disc ratio was 0.40 to 0.74 (mean 0.49 ± 0.14) in the patient group, and 0.23 to 0.47 (mean 0.39 ± 0.09) in the control group. The mean axial length was 22.89 to 26.16 mm (mean 25.1 ± 1.4 mm) in the patient group, and 22.88 to 25.98 mm (mean 24.5 ± 1.2 mm) in the control group.

All subjects went through a full eye examination by an ophthalmologist before the imaging sessions. Consent forms were signed by each subject, after a full explanation of procedures and consequences of this study. All studied eyes were dilated using 0.5% tropicamide. The study protocol was approved by Indiana University Institutional Review Board and is in accordance with the Declaration of Helsinki.

The Indiana AOSLO With Clinical Planning Module

The wide-field AOSLO equipped with a clinical planning module[30] has been presented previously. In brief, the AOSLO used a super-continuum laser source (NKT Photonics, Birkerød, Denmark) as the illumination source, which can provide imaging wavelengths from 450 to 900 nm, although we only used 820 to 840 nm in this study. The AOSLO uses two deformable mirrors and a wave-front sensor to correct ocular monochromatic aberrations in a close-loop feedback system. The imaging field is approximately 2° × 1.8° and can be steered over at least 20° on the retina. A digital projector was incorporated in the system to provide a programmable fixation target for subjects. To image retinal regions larger than 2° × 1.8°, it is necessary to steer the AOSLO imaging beam across the retina, acquiring sequential video images at multiple positions to cover the area of interest.

Procedures

Imaging. An imaging session consisted of three portions. First, the axial length was measured with an IOLMaster (Carl Zeiss Meditec, Dublin, CA, USA). Second, the eye was imaged with a Heidelberg Spectralis SLO/OCT system (Heidelberg Engineering, Heidelberg, Germany), and, third, the eye was imaged with the AOSLO.

For SLO/OCT imaging, we first obtained 30° × 30° SLO images with the Spectralis, which are centered at the fovea and at approximately 12° temporal to the fovea, respectively. These two images were used to construct a mosaic fundus image using the Heidelberg built-in software, as indicated in Figure 1. Then, we performed OCT imaging in the temporal retina and macular region. For the temporal retina, the OCT imaging field size was 15° horizontally by 15° vertically, and the imaging field was centered at approximately 12° temporal to the fovea. Each B-scan was oriented in the vertical direction. The distance between adjacent B-scans was 60 μm. The macular region was imaged using two perpendicular OCT volume scans to allow accurate localization of the fovea. The first used vertical B-

Investigative Ophthalmology & Visual Science

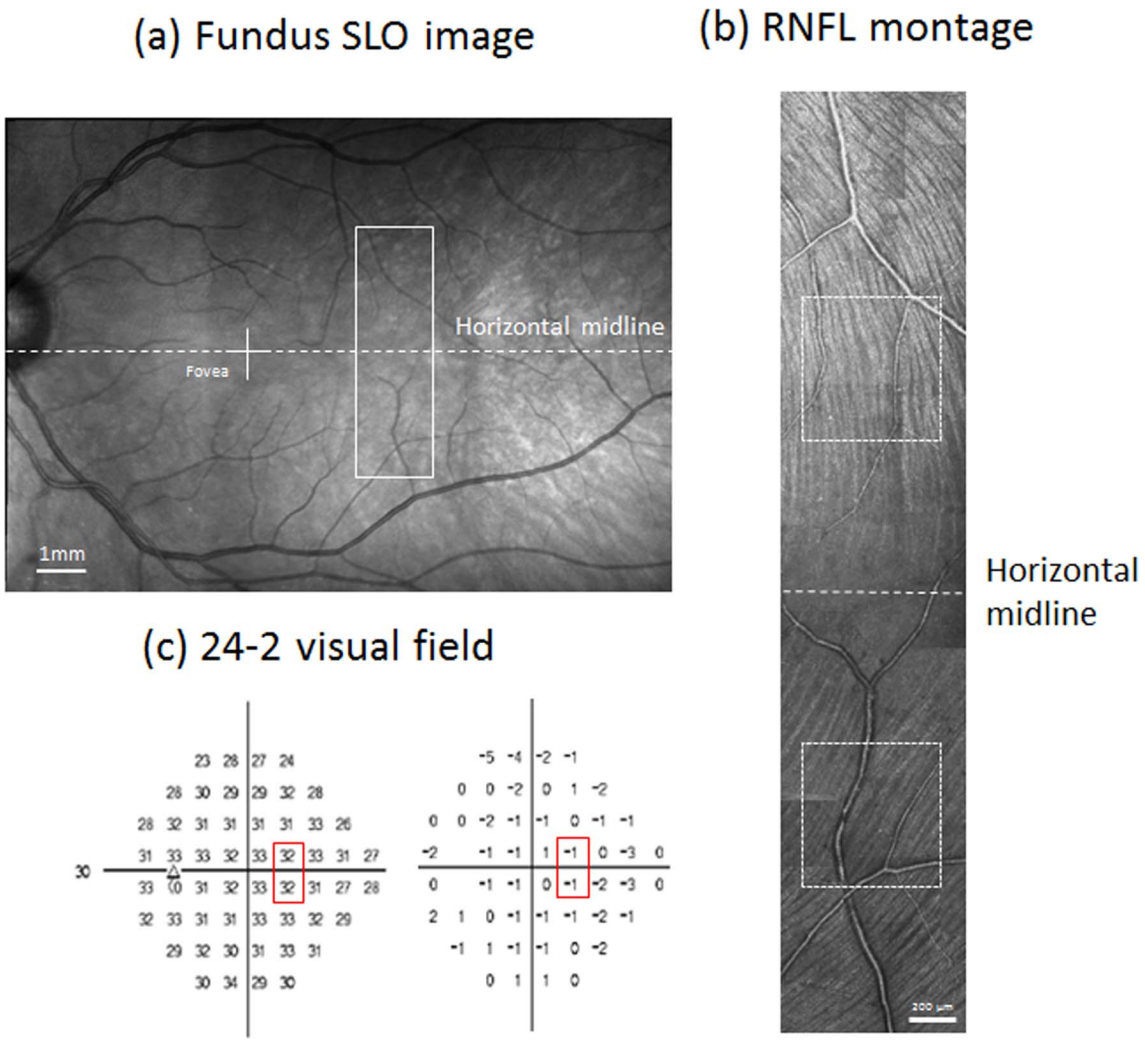

Figure 2. (**a**) A wide-field fundus mosaic of a control subject. The *white cross* indicates the fovea. The *white box* with *solid lines* indicates approximately where AOSLO imaging was performed. The *horizontal dashed line* is the horizontal midline of the retina drawn through the fovea and defines the horizontal midline for the visual field. (**b**) The RNFL montage of the same control subject constructed from AOSLO images. Brightness of each image was adjusted to minimize the transition between images. The *white boxes* indicate regions where the bundle index was computed for this subject (see text for details). The *dashed line* indicates the midline of the retina. (**c**) Sensitivity map (*left*) and TD map (*right*) of a 24-2 visual field for the same control subject. The *red boxes* indicate the stimulus locations that fell within the AOSLO imaging region.

scans and the other had horizontal B-scans. The scanning size was 15° × 5°. Adjacent B-scans were separated by 30 μm. Imaging locations for OCT are indicated in Figure 1.

For AOSLO imaging, the imaging region was centered approximately 9° temporal to the fovea, and the size of the region was at least 10° vertically by 4° horizontally. For each imaging field location, the AOSLO collected 75 images at a 30-Hz frame rate. The adjacent fields had approximately 0.5° or more of overlap. Subjects were allowed to take breaks during imaging. The whole procedure for AOSLO imaging including the subject's break time took between 20 and 50 minutes depending on the subject.

Postprocessing of AOSLO Images and Formation of Montages. Removal of eye movements and averaging of video frames were performed in MATLAB (The Mathworks, Inc., Natick, MA, USA). Montages were then created manually using Photoshop CS6 (Adobe Systems, Inc., San Jose, CA, USA). Images from spatially adjacent regions were first aligned. Then, for each raw montage, we adjusted the brightness of images to match neighboring images visually, using a Photoshop built-in brightness adjustment, which is a linear process. Finally, we used Photoshop to manually register the resulting AOSLO montage with the wide-field SLO image acquired by the Spectralis (see Figs. 2a, 2b).

Alignments Between the AOSLO, OCT, and Visual Field. To compare outcomes that were acquired from these three techniques, it was necessary to set up a common coordinate system. This was performed in two steps. First, the fovea was identified in SLO/OCT images. Using the horizontal and vertical OCT cross sections of the fovea, we identified the center of the foveal depression and referred this to the SLO image using Heidelberg's built-in OCT/SLO display. Next, we assumed that the horizontal scan of the OCT/SLO corresponded to the horizontal axis of the visual field, and thus we could equate the visual field location to the OCT/SLO images and measurements. The AOSLO montages had been registered to SLO images and thus can be related to the visual field locations by using SLO images as bridges.

Regions/Locations of Measurements. For visual fields, we selected the one at 9° nasal, 3° superior field, and the one at 9° nasal, 3° inferior field for analysis. For each AOSLO montage, we picked two regions that are central to these two visual field

Investigative Ophthalmology & Visual Science

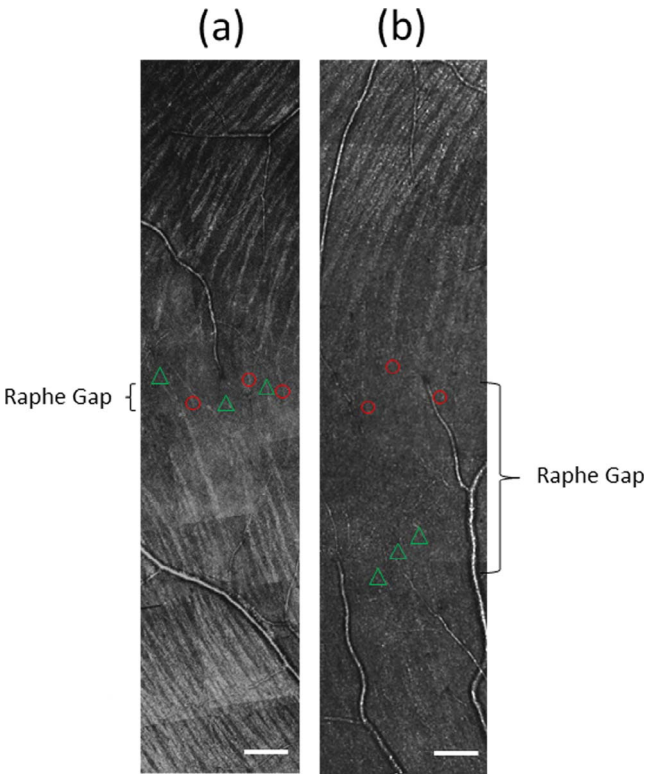

FIGURE 3. Example of nerve fiber imaging and the raphe gap measurements in a normal and glaucomatous eye. (**a**) The AOSLO montage of the temporal raphe in a control subject. (**b**) A raphe image from a patient with a nasal step. Contrast of these two montages was adjusted to further enhance the visualization of bundles for readers. The TD of field sensitivity was −0.67 dB corresponding to the superior part of the montage where the nerve fiber bundles are still visible. The TD was −1.67 dB corresponding to the inferior part of the montage, where nerve fiber bundles are barely seen. The raphe gap in (**b**) is larger than in (**a**). For both images, the *red circles* and *green triangles* represent where the visible ends of RNFL bundles were marked by human graders. *Scale bar*: 200 μm.

locations respectively. The size of each region was set as approximately 2 × 2 degrees. For OCT B-scan images that were across each region, we selected one image that is closest to the center of the region, and on each side of this image, we selected one image that was approximately 180 μm away. The parts of these three OCT images that fall in the region were used for further analysis.

Quantitative Measurements

Measurement of the Raphe Gap. For each RNFL AOSLO montage, we manually measured the raphe gap defined as the vertical distance between the boundaries of visible superior and inferior nerve fiber bundles. Specifically, for each side of the raphe (superior or inferior), a grader, masked to all relevant clinical information including all visual field reports and diagnostic reports, identified the three longest bundles that could be observed in the montage. Then, the tip of each bundle was marked, and their averaged vertical position was used as the boundary for the side. The raphe gap of a given eccentricity was then computed as the mean vertical distance between the superior and inferior bundle boundaries at that eccentricity (e.g., Fig. 3). To compare data across subjects, distances were adjusted for individual differences in axial length, according to the Gullstrand model eye. To improve the reliability of the grading we had two graders independently make these measurements and used the averaged results. Note that the measured raphe gap may not necessarily represent a region totally lacking bundles and axons. The diameters of ganglion cell axons in the RNFL can range from 0.1 μm to more than 2 μm,[34,35] and thus axons and bundles could be unrecognizable in AOSLO images. Thus, the measured gap could contain axons too small to be resolved. That is, our measurements could be larger than the "true gap" lacking any bundles; however, this same limitation is present for both glaucomatous and control eyes, assuming the optics and other aspects controlling the contrast of images are similar and are independent of glaucoma.

Measurement of Bundle Reflectivity and Density by Bundle Index. To evaluate the reflectivity and density of RNFL bundles, we developed an image descriptor we named the "bundle index." The bundle index captures the response of steerable first-order Gaussian derivative filters[36] (see Fig. 4). These filters are designed for extracting oriented edge contrast in an image and thus are suitable to extract the relative reflectivity of oriented RNFL bundle patterns by computing the contrast between the bundle area and its adjacent nonbundle area. Information about density of RNFL bundles can be incorporated by integrating these filters' responses over a larger region.

Although absolute reflectivity seems a more direct descriptor for bundles, in practice the absolute reflectivity would be affected by a number of factors that are difficult to control during imaging. Two obvious factors are media clarity in aging eyes and illumination power difference between different imaging sessions. In contrast, relative reflectivity has the advantage that it essentially normalizes for some of these individual sources of variation, by comparing the relative reflectivity of bundles with adjacent nonbundle areas. If we assume that nonbundle regions are not affected by glaucoma, then relative reflectivity is directly related to absolute reflectivity of bundles.

For a given RNFL region in AOSLO montages, we computed a bundle index in MATLAB using the following six steps. First, we created a set of steerable first-order two-dimensional Gaussian filters containing 12 orientations (0 to 165° in 15° steps) at each of 15 spatial scales. The size of the filter is defined as the distance between the pixel of the most positive intensity and the pixel of the most negative intensity. The spatial scales of the filters were varied such that the size of the filters ranged from 8 to 22 μm in 1 μm steps. Second, each set of filters was then convolved with the RNFL region, generating a filter response series for each pixel. Normalization was performed by dividing pixel responses over the averaged intensity of the local region that the filter was convolved with. Third, pixels containing blood vessels or on boundaries between neighboring images were manually marked as invalid. Correspondingly, the filter responses obtained in the previous step in which these invalid pixels were involved were also marked as invalid to reduce responses that are irrelevant to bundles. For image boundaries, the responses are high because we manually adjusted image brightness during montage construction, and therefore the brightness transition between neighboring images could be unsmooth, forming artificial contrast and high filter responses. Fourth, the response at each orientation for the whole region was then computed by averaging the responses of that orientation from all valid pixels within the region. Fifth, the bundle index for each size of filter was computed as the absolute difference between maximum and minimum orientation responses of that given size of filter. Sixth, the maximum bundle index across filter sizes was then used as the bundle index for the region. Figure 4 presents two examples of this process. One example contains an image with

Investigative Ophthalmology & Visual Science

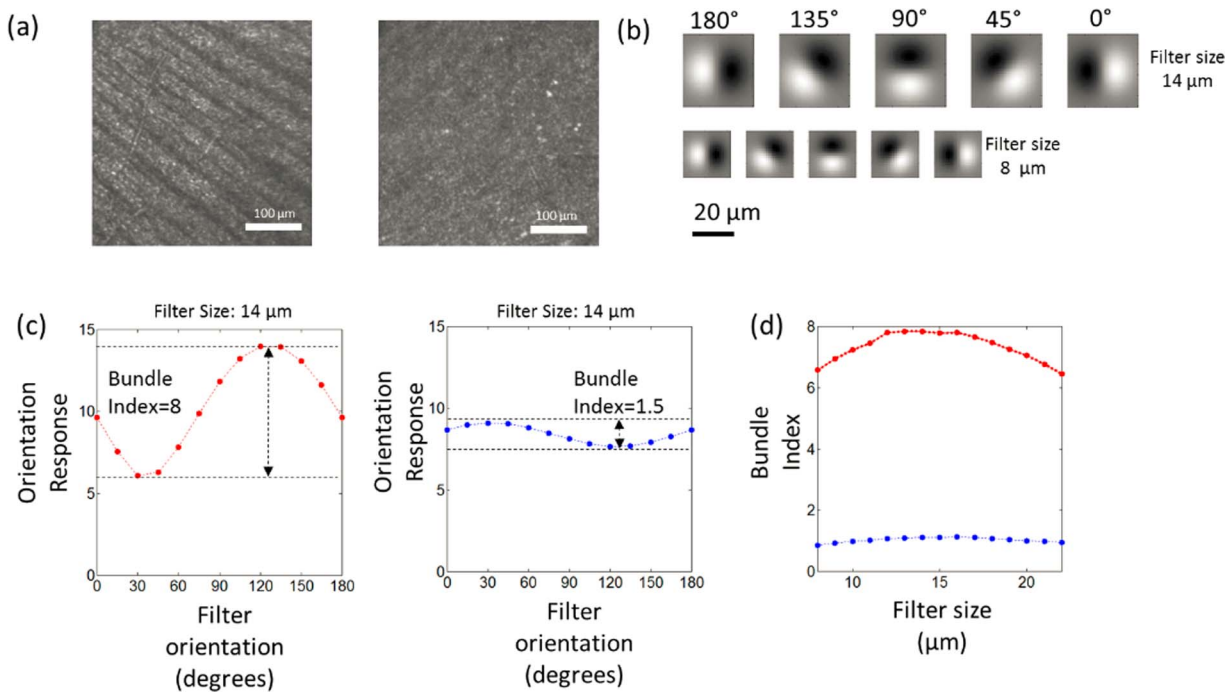

Figure 4. Illustration of bundles index computation. (**a**) Two RNFL images. Nerve fiber bundles are reflective in the left image and barely recognizable in the right image. (**b**) The spatial profiles for two sets of steerable Gaussian filters with two different sizes. See text for definition of filter size. For illustration purpose, we only show five orientations of each set. (**c**) The orientation responses when the first filter set in (**b**) is convolved with each image in (**a**). See text for details of computation. The *red line* in the left graph represents the responses from the left image in (**a**), and the *blue line* in the right graph presents the responses from the right image in (**a**). The difference between the maximum and minimum orientation responses of each filter set is the bundle index for this filter set. (**d**) The bundle index changes across all filter sizes for both images in (**a**). The *red curve* on the top corresponds to the left image in (**a**). The *blue curve* corresponds to the right image in (**a**). The maximum bundle index across filter sizes is used for further quantitative analysis.

highly reflective bundles and the other with barely visible bundles.

Measurement of RNFL and GCC Thickness. For a given region in an OCT B-scan image, the boundaries of the RNFL and GCC were identified manually. The thickness of the RNFL and GCC for the region were then computed and averaged. To improve the reliability of measurements, we had two graders independently make the segmentation and averaged the results.

Visual Field. For the 24-2 visual field, two test locations fall on the region that was imaged using the AOSLO imaging: the one at 9° nasal, 3° superior field, and the one at 9° nasal, 3° inferior field.

For each subject, we computed total deviation (TD) for each of these two test locations by averaging the TDs for that location from three visual field tests over an interval of approximately 6 months. To compare the field loss with the raphe gap, we further averaged the values of these two test locations for each studied eye because only one raphe gap was obtained for the corresponding region. In particular, for each studied eye, the antilog values of TD for these two locations were averaged, and then logged. This logged value was defined as averaged field loss. This computation was consistent with how other studies calculated averaged TD over regions.[37–40]

Statistics

We used both unpaired *t*-tests and Mann-Whitney *U* tests to compare the bundle index, RNFL thickness, GCC thickness, and raphe gap between the patients and controls. To minimize Type 1 errors when using multiple tests, a *P* value of 0.0125 was used for statistical significance. Two-way random intraclass correlation coefficient (ICC) with absolute agreement was used to assess the reliability of measurements of RNFL thickness, GCC thickness, as well as raphe gap.[41]

Results

Difference in RNFL Appearance Between Glaucomatous and Control Eyes

The appearance of the RNFL differed between control and glaucomatous eyes. In control eyes, nerve fiber bundles were highly reflective and readily distinguished from the spaces between bundles. In contrast, bundles in glaucomatous eyes were often less crisp in appearance and the boundaries with the spaces between bundles were less sharply defined. The raphe gap in glaucomatous eyes appeared different from control subjects, with a notable lack of nerve fiber bundles near the raphe, although they could often be seen further from the raphe (Fig. 5). Within the raphe gap, we did not see any reflective source, other than blood vessels, that showed reflectance comparable to the reflectance of bundles.

Quantitative Differences Between Glaucomatous and Control Eyes

The averaged field loss, which is the average of the total six visual field points in three visual field reports, as defined above, was lower in the patient group than in the control group (–1.48 ± 1.13 dB, as opposed to 0.18 ± 0.65 dB; *t*-test $P = 0.002$, Mann-Whitney *U* test $P = 0.005$). The raphe gap was larger in glaucomatous eyes than control eyes (585.1 ± 281.3 µm versus 230.8 ± 107.2 µm; *t*-test $P < 0.0001$, Mann-Whitney *U* test $P = 0.001$). The bundle index was smaller in

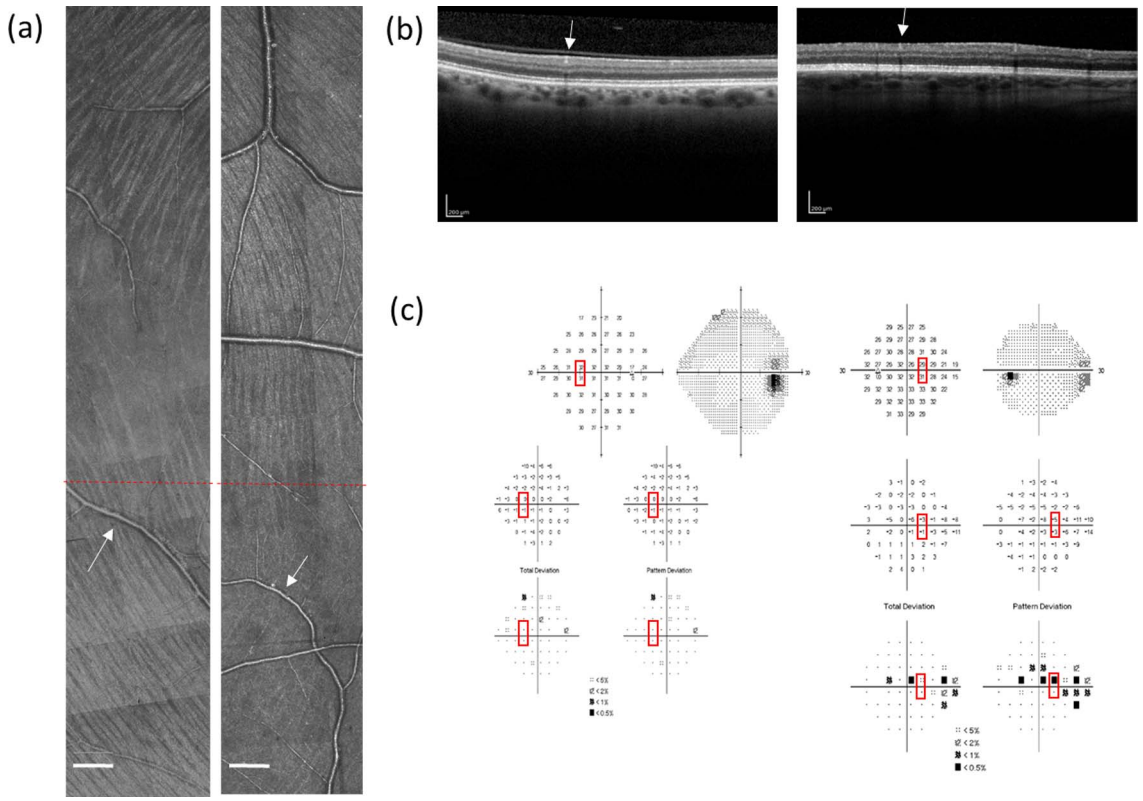

Figure 5. Example of AOSLO montages, OCT images, and visual fields from two subjects. (**a**) The RNFL montages constructed from AOSLO images. The left image is from a control subject and the right from a patient, where bundles are barely observed in the lower half of the image. *Red dashed lines* in both montages indicate the horizontal midline. *Scale bar*: 200 μm. (**b**) Optical coherence tomography images in the same region. *Left* is from the control and the *right* is from the patient. The *white arrows* in (**a**) and (**b**) point to the same vessels in AO montages and OCT images. (**c**) Corresponding 24-2 visual field reports. Left and right are from the control and the patient respectively. *Red boxes* indicate testing locations that fall within the region of the AOSLO imaging. For the control, the averaged TD over three reports (visits) was −0.67 dB at 9° nasal, 3° superior field, and −1 dB at 9° nasal, 3° inferior field. For the patient, the corresponding averaged TD over three reports (visits) was −2.33 dB at 9° nasal, 3° superior field, and −0.33 dB at 9° nasal, 3° inferior field.

glaucomatous eyes than control eyes (2.8 ± 1.9 versus 4.9 ± 1.9; *t*-test $P = 0.0025$, Mann-Whitney U test $P = 0.004$). The RNFL thickness as measured with OCT was thinner in glaucomatous eyes than control eyes (20.38 ± 5.24 μm versus 23.324 ± 3.07 μm; *t*-test $P = 0.032$, Mann-Whitney U test $P = 0.087$). The GCC thickness was thinner in glaucomatous eyes than controls (68.56 ± 25.20 μm versus 80.16 ± 18.28 μm; *t*-test $P < 0.0001$, Mann-Whitney U test $P = 0.0001$). The ICC was 0.96 (95% confidence interval [CI] 0.88–0.98) for measurements of raphe gap, 0.73 (95% CI 0.53–0.85) for measurements of RNFL thickness, and 0.95 (95% CI 0.90–0.97) for measurements of GCC thickness. The mean measurement difference between the two graders was 4.52 ± 44.71 μm for measurements of the raphe gap, 0.04 ± 0.84 μm for RNFL thickness, and 0.13 ± 0.81 μm for GCC thickness.

The raphe gap was larger for patients with greater field loss, as shown in Figure 6a. Eight of nine eyes showed larger raphe gaps than all the control eyes. The bundle index, RNFL thickness, and GCC thickness exhibit large individual variability between subjects, as shown in Figures 6b through 6d. For two glaucomatous eyes with more than −5 dB TD, results of all these measurements were smaller than ones for all other glaucomatous eyes as well as control eyes.

Discussion

The results of the study provide evidence that structural changes occur to the temporal raphe even when local functional loss is mild. Although the decreased bundle index taken alone could be explained by either decreased reflectivity or low density of remaining bundles, the enlarged raphe gap and reduced GCC thickness suggest that there is a loss of the bundles and ganglion cells in this area. More importantly, we found statistically significant differences in three of four measurements, even when the local TD of the field sensitivity was relatively small and subject number for the study was small. In particular, the enlarged raphe gap was found in eight of nine glaucomatous eyes with local averaged field loss no worse than −3.5 dB.

Finding statistically differences between these two small groups can be partially attributed to the fact that ganglion cell axons are close to their cell bodies in the temporal raphe, and therefore visual field sensitivities can be mapped more accurately to the RNFL arising from ganglion cells with receptive fields in this region and have more direct relation to structural changes.

The three measurements that showed statistically significant differences between control and patient groups each have their own strengths and weakness. The lack of detectable nonvessel residual tissue within the increased raphe gap suggests that measuring the raphe gap in en face plane is relatively insensitive to effects of RNFL remnants. It has been shown that, for eyes under conditions of severe field loss, the residual RNFL thicknesses in the peripapillary region were still approximately 33% or more of the mean values for healthy eyes,[40] and showed considerable variation between individu-

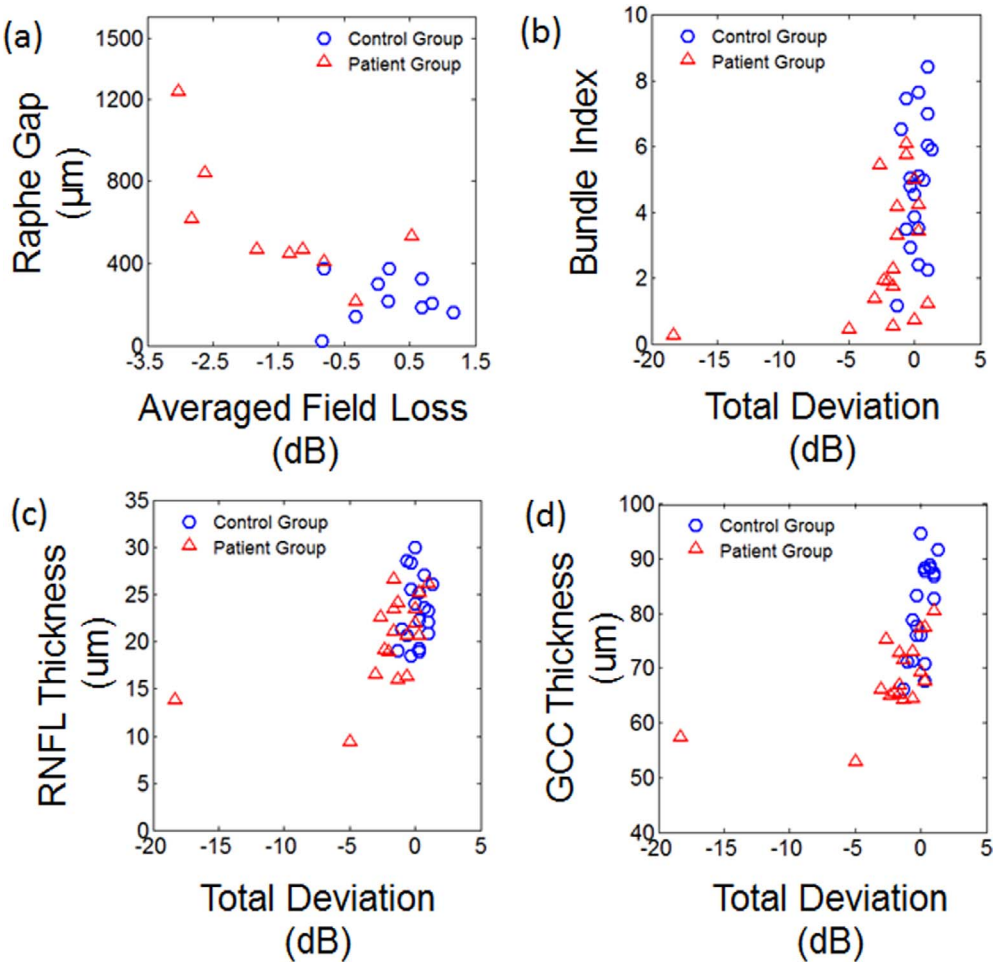

Figure 6. Comparison of imaging measurements to local visual field results. (**a**) Raphe gap as a function of averaged field loss. (**b**) Bundle index as a function of TD. (**c**) The RNFL thickness as a function of TD. (**d**) The GCC thickness as a function of TD. *Blue circles* represent data of the controls and the *red triangles* represent data of the patients with glaucoma. The two groups in (**a**, **b**, **d**) are significantly different, with *P* value less than 0.0001 in (**a**), equal to 0.0018 in (**c**), and (**d**), with *P* values less than the α value 0.0125.

als. This could further complicate the evaluation of loss in RNFL thickness around the optic disc in patients with glaucoma. In contrast, this did not become a challenge for evaluation of the raphe gap.

Although there are various possible reasons for this, we suggest that the RNFL in the temporal raphe, which is thinner than in most of the retina, has a lower requirement for the support from glial cells. This can be supported by the histological finding that astrocytes, which are a major glial component of RNFL bundles,[42–45] were found at high density near the optic disc region, and their density fell when the RNFL becomes thin.[44,46,47]

In contrast to the raphe gap, which describes only one property of the RNFL, the bundle index combines multiple properties of the RNFL into only one number. This is because theoretically the AOSLO with a proper optical configuration can achieve an axial resolution of approximately 50 to 75 μm.[48,49] This axial range is slightly larger than or equal to the RNFL thickness in this region. As a result, pixels in AOSLO images may contain information about both bundle intrinsic properties and bundle density along the depth. During bundle index computation, we integrated filter responses over a region, which further incorporated information on en face bundle density, providing us with a descriptor that, while localized, still incorporated information averaged over a region of RNFL in all three dimensions. An obvious tradeoff for this measurement is that we are not able to decouple changes in individual properties of the RNFL. Future studies are needed to explore the optimal use of the index.

Compared with the first two measurements that reflect changes only in the RNFL, the measurement of the GCC adds information about ganglion cells and has potential to explore how ganglion cells are affected in this region in future studies.

Compared with the GCC measurement, measuring the thickness of the RNFL is relatively challenging. The RNFL thickness corresponded to only 4 to 8 pixels in OCT images of the control group, and the averaged thickness difference between the two groups was only approximately 4 μm, which was equivalent to approximately 1 pixel in images. Therefore RNFL thickness measurements exhibited a limited dynamic range. Even worse, the contrast of the RNFL layer relative to ganglion cell layer was low, which further increases the difficulty of RNFL segmentation. To increase the accuracy of measuring RNFL thickness changes, an OCT imaging system with higher axial resolution is necessary.

The between-subject variability of the bundle index as well as RNFL and GCC thickness in our control group was large. This could be partially attributed to the fact that we compared locations at equal distances above and below the horizontal midline of the retina, but there is considerable between-subject variability in how far the raphe deviates from the horizontal midline of the retina.[31,32] Future studies are warranted to

investigate how the raphe's deviation from the horizontal midline affects the variability of the measurements.

Our study was restricted to only a small portion of the raphe due to the small imaging fields of the current AOSLO. This could be improved by using an AOSLO with larger field.[50] Also, it is worth pointing out that AOSLO is not the only means to image the RNFL in the raphe. The improved en face OCT technique is able to extract en face information of the temporal raphe,[32] although en face resolution of OCT is lower than AOSLO. Future research is needed to explore and compare the capabilities of both imaging approaches for glaucoma assessment.

In conclusion, structural changes occur to the temporal raphe even when local functional loss is mild. These changes can be visualized and measured using high-resolution imaging techniques and proper metrics. The study opens the possibility of using the temporal raphe as a site for glaucoma research and clinical assessment.

Acknowledgments

Supported by National Institutes of Health Grants R01 EY04395 (SAB), R01 P30EY019008 (SAB), R01 EY007716, and R01 EY024542 (WHS). The authors alone are responsible for the content and writing of the paper.

Disclosure: **G. Huang**, None; **T. Luo**, None; **T.J. Gast**, None; **S.A. Burns**, Nidek (C); **V.E. Malinovsky**, None; **W.H. Swanson**, None

References

1. Heijl A, Lindgren A, Lindgren G. Test-retest variability in glaucomatous visual fields. *Am J Ophthalmol*. 1989;108:130–135.
2. Piltz JR, Starita RJ. Test-retest variability in glaucomatous visual fields. *Am J Ophthalmol*. 1990;109:109–111.
3. Artes PH, Iwase A, Ohno Y, Kitazawa Y, Chauhan BC. Properties of perimetric threshold estimates from Full Threshold, SITA Standard, and SITA Fast strategies. *Invest Ophthalmol Vis Sci*. 2002;43:2654–2659.
4. Hoyt WF, Frisen L, Newman NM. Fundoscopy of nerve fiber layer defects in glaucoma. *Invest Ophthalmol*. 1973;12:814–829.
5. Airaksinen PJ, Alanko HI. Effect of retinal nerve fibre loss on the optic nerve head configuration in early glaucoma. *Graefes Arch Clin Exp Ophthalmol*. 1983;220:193–196.
6. Airaksinen PJ, Drance SM, Douglas GR, Mawson DK, Nieminen H. Diffuse and localized nerve fiber loss in glaucoma. *Am J Ophthalmol*. 1984;98:566–571.
7. Airaksinen PJ, Drance SM, Douglas GR, Schulzer M, Wijsman K. Visual field and retinal nerve fiber layer comparisons in glaucoma. *Arch Ophthalmol*. 1985;103:205–207.
8. Sommer A, D'Anna SA, Kues HA, George T. High-resolution photography of the retinal nerve fiber layer. *Am J Ophthalmol*. 1983;96:535–539.
9. Rohrschneider K, Burk RO, Kruse FE, Volcker HE. Reproducibility of the optic nerve head topography with a new laser tomographic scanning device. *Ophthalmology*. 1994;101:1044–1049.
10. Wollstein G, Garway-Heath DF, Hitchings RA. Identification of early glaucoma cases with the scanning laser ophthalmoscope. *Ophthalmology*. 1998;105:1557–1563.
11. Dreher AW, Reiter K. Retinal laser ellipsometry: a new method for measuring the retinal nerve-fiber layer thickness distribution. *Clin Vis Sci*. 1992;7:481–488.
12. Schuman JS, Hee MR, Arya AV, et al. Optical coherence tomography: a new tool for glaucoma diagnosis. *Curr Opin Ophthalmol*. 1995;6:89–95.
13. Liang J, Williams DR, Miller DT. Supernormal vision and high-resolution retinal imaging through adaptive optics. *J Opt Soc Am A Opt Image Sci Vis*. 1997;14:2884–2892.
14. Takayama K, Ooto S, Hangai M, et al. High-resolution imaging of retinal nerve fiber bundles in glaucoma using adaptive optics scanning laser ophthalmoscopy. *Am J Ophthalmol*. 2013;155:870–881.
15. Chen MF, Chui TY, Alhadeff P, et al. Adaptive optics imaging of healthy and abnormal regions of retinal nerve fiber bundles of patients with glaucoma. *Invest Ophthalmol Vis Sci*. 2015;56:674–681.
16. Wirtschafter JD, Becker WL, Howe JB, Younge BR. Glaucoma visual-field analysis by computed profile of nerve-fiber function in optic disk sectors. *Ophthalmology*. 1982;89:255–267.
17. Yamagishi N, Anton A, Sample PA, Zangwill L, Lopez A, Weinreb RN. Mapping structural damage of the optic disk to visual field defect in glaucoma. *Am J Ophthalmol*. 1997;123:667–676.
18. Anton A, Yamagishi N, Zangwill L, Sample PA, Weinreb RN. Mapping structural to functional damage in glaucoma with standard automated perimetry and confocal scanning laser ophthalmoscopy. *Am J Ophthalmol*. 1998;125:436–446.
19. Weber J, Dannheim F, Dannheim D. The topographical relationship between optic disk and visual-field in glaucoma. *Acta Ophthalmol (Copenh)*. 1990;68:568–574.
20. Garway-Heath DF, Poinoosawmy D, Fitzke FW, Hitchings RA. Mapping the visual field to the optic disc in normal tension glaucoma eyes. *Ophthalmology*. 2000;107:1809–1815.
21. Denniss J, Turpin A, McKendrick AM. Individualized structure-function mapping for glaucoma: practical constraints on map resolution for clinical and research applications. *Invest Ophthalmol Vis Sci*. 2014;55:1985–1993.
22. Jansonius NM, Schiefer J, Nevalainen J, Paetzold J, Schiefer U. A mathematical model for describing the retinal nerve fiber bundle trajectories in the human eye: average course, variability, and influence of refraction, optic disc size and optic disc position. *Exp Eye Res*. 2012;105:70–78.
23. Lamparter J, Russell RA, Zhu H, et al. The influence of intersubject variability in ocular anatomical variables on the mapping of retinal locations to the retinal nerve fiber layer and optic nerve head. *Invest Ophthalmol Vis Sci*. 2013;54:6074–6082.
24. Curcio CA, Allen KA. Topography of ganglion-cells in human retina. *J Comp Neurol*. 1990;300:5–25.
25. Drasdo N, Millican CL, Katholl CR, Curcio CA. The length of Henle fibers in the human retina and a model of ganglion receptive field density in the visual field. *Vision Res*. 2007;47:2901–2911.
26. Werner EB, Drance SM. Early visual field disturbances in glaucoma. *Arch Ophthalmol*. 1977;95:1173–1175.
27. Hart WM Jr, Becker B. The onset and evolution of glaucomatous visual field defects. *Ophthalmology*. 1982;89:268–279.
28. Lee AJ, Wang JJ, Rochtchina E, Healey P, Chia EM, Mitchell P. Patterns of glaucomatous visual field defects in an older population: the Blue Mountains Eye Study. *Clin Exp Ophthalmol*. 2003;31:331–335.
29. Armaly MF. Visual field defects in early open angle glaucoma. *Trans Am Ophthalmol Soc*. 1971;69:147–162.
30. Huang G, Qi X, Chui TY, Zhong Z, Burns SA. A clinical planning module for adaptive optics SLO imaging. *Optom Vis Sci*. 2012;89:593–601.
31. Huang G, Gast TJ, Burns SA. In-vivo adaptive optics imaging of the temporal raphe and its relationship to the optic disc and fovea in the human retina. *Invest Ophthalmol Vis Sci*. 2014;55:5952–5961.

32. Chauhan BC, Sharpe GP, Hutchison DM. Imaging of the temporal raphe with optical coherence tomography. *Ophthalmology*. 2014;121:2287–2288.
33. Swanson WH, Malinovsky VE, Dul MW, et al. Contrast sensitivity perimetry and clinical measures of glaucomatous damage. *Optom Vis Sci*. 2014;91:1302–1311.
34. FitzGibbon T, Taylor SF. Mean retinal ganglion cell axon diameter varies with location in the human retina. *Jpn J Ophthalmol*. 2012;56:631–637.
35. Ogden TE. Nerve-fiber layer of the primate retina: morphometric analysis. *Invest Ophthalmol Vis Sci*. 1984;25:19–29.
36. Freeman WT, Adelson EH. The design and use of steerable filters. *IEEE Trans Pattern Anal Mach Intell*. 1991;13:891–906.
37. Hood DC, Zhang X. Multifocal ERG and VEP responses and visual fields: comparing disease-related changes. *Doc Ophthalmol*. 2000;100:115–137.
38. Hood DC, Greenstein VC. Multifocal VEP and ganglion cell damage: applications and limitations for the study of glaucoma. *Prog Retin Eye Res*. 2003;22:201–251.
39. Hood DC, Anderson SC, Wall M, Kardon RH. Structure versus function in glaucoma: an application of a linear model. *Invest Ophthalmol Vis Sci*. 2007;48:3662–3668.
40. Hood DC, Kardon RH. A framework for comparing structural and functional measures of glaucomatous damage. *Prog Retin Eye Res*. 2007;26:688–710.
41. Shrout PE, Fleiss JL. Intraclass correlations: uses in assessing rater reliability. *Psychol Bull*. 1979;86:420–428.
42. Trivino A, Ramirez JM, Salazar JJ, Ramirez AI, Garcia-Sanchez J. Immunohistochemical study of human optic nerve head astroglia. *Vision Res*. 1996;36:2015–2028.
43. Ogden TE. Nerve fiber layer of the primate retina: thickness and glial content. *Vision Res*. 1983;23:581–587.
44. Ogden TE. Nerve fiber layer astrocytes of the primate retina: morphology, distribution, and density. *Invest Ophthalmol Vis Sci*. 1978;17:499–510.
45. Bussow H. The astrocytes in the retina and optic nerve head of mammals: a special glia for the ganglion cell axons. *Cell Tissue Res*. 1980;206:367–378.
46. Reichenbach A. Quantitative and qualitative morphology of rabbit retinal glia. A light microscopical study on cells both in situ and isolated by papaine. *J Hirnforsch*. 1987;28:213–220.
47. Stone J, Dreher Z. Relationship between astrocytes, ganglion cells and vasculature of the retina. *J Comp Neurol*. 1987;255:35–49.
48. Gray DC, Wolfe R, Gee BP, et al. In vivo imaging of the fine structure of rhodamine-labeled macaque retinal ganglion cells. *Invest Ophthalmol Vis Sci*. 2008;49:467–473.
49. Venkateswaran K, Roorda A, Romero-Borja F. Theoretical modeling and evaluation of the axial resolution of the adaptive optics scanning laser ophthalmoscope. *J Biomed Opt*. 2004;9:132–138.
50. Mujat M, Ferguson RD, Iftimia N, Hammer DX. Compact adaptive optics line scanning ophthalmoscope. *Opt Express*. 2009;17:10242–10258.

Investigative Ophthalmology & Visual Science